ACS APPLIED NANO MATERIALS

www.acsanm.org Article

Enhanced Room-Temperature NH_3-Sensing Performance of $Ti_3C_2T_x$ MXene Decorated with CeO_2 Nanoparticles

Lizhai Zhang,* Jiayuan Xu, Dingyuan Wang, Xinyu Lei, Henghui Sun, Yuhong Huang, Fei Ma, Taotao Ai,* and Paul K. Chu*

Cite This: *ACS Appl. Nano Mater.* 2025, 8, 12090−12099 Read Online

ACCESS | Metrics & More | Article Recommendations | Supporting Information

ABSTRACT: 2D MXenes have garnered enormous interest in the field of gas sensing. Unfortunately, the low stability, long recovery time, poor selectivity, and vulnerability to oxidation have hampered further development. Herein, $Ti_3C_2T_x$ MXene is incorporated with CeO_2 nanoparticles to improve the detection of NH_3. Compared with $Ti_3C_2T_x$ and CeO_2, the response of composite to 10 ppm of NH_3 is enhanced by 180% and 714% at room temperature, respectively, in addition to the excellent selectivity, fast response, and recovery rate. Based on the first-principles calculation, the CeO_2 nanoparticles form a multifunctional passivation layer to shield the MXene from oxidative degradation and also provide ample active sites to adsorb NH_3 gas to enhance the sensing ability. The results reveal an effective means of designing and developing high-performance room-temperature ammonia sensors.

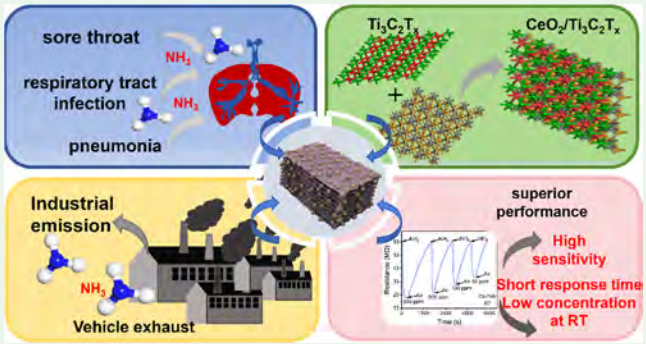

KEYWORDS: *CeO_2, $Ti_3C_2T_x$, heterojunction, room-temperature gas sensor, first-principles calculation*

1. INTRODUCTION

Ammonia (NH_3) emitted into the atmosphere during the industrial process of synthesizing chemical manure, plastics, and synthetic fibers not only causes the serious water ecosystem pollution but also constitutes to the generation of suspended particles ($PM_{2.5}$) in the atmosphere. Furthermore, higher NH_3 concentration in air can cause severe health problems, including vomiting, headaches, pulmonary edema, and so on.[1−5] In addition, metabolic activities in humans generate NH_3 gas, and kidney diseases can be diagnosed by detection of NH_3.[5] Hence, the development of sensing materials highly sensitive to NH_3 is crucial for human health and environmental protection.

In the past decades, various NH_3-sensing materials, such as metal oxide, transition metal dichalcogenide (TMDCs), and polymers, have been applied for detection of NH_3.[6−11] However, the high working temperature limits the application of metal oxide.[10] The TMDCs and polymers always suffer from the poor recovery performance, low stability, and low response at room temperature (RT).[9−11] Hence, it is urgent to develop new NH_3-sensing materials with high sensing performance. $Ti_3C_2T_x$, as an typical class of MXene, possesses excellent electrical conductivity, high signal-to-noise ratio, and abundant surface functional groups, boding well for NH_3 monitoring at RT.[12−16] Because of the active surface groups (−O, −OH, −F) and metal layers, $Ti_3C_2T_x$ shows exceptional electrical conductivity, promoting interaction with NH_3 molecular. For example, Lee et al. synthesized $Ti_3C_2T_x$ by etching the Ti_3AlC_2 with HCI and LiF mixture and observed that $Ti_3C_2T_x$ showed the higher response to NH_3 at RT compared to ethanol, methanol, and acetone.[12] Wu et al. found that the response of $Ti_3C_2T_x$ toward 500 ppm of NH_3 was about 6.13%, which is four times higher than ethanol (1.5%).[14] Yang et al. successfully prepared alkalized $Ti_3C_2T_x$ by using NaOH, and the 100 ppm of NH_3-sensing response was enhanced to 28.87% at RT.[15] However, because of strong interlayer van der Waals forces, the $Ti_3C_2T_x$ suffers from restacking and agglomeration, causing the loss of active sites and consequently limiting the NH_3-sensing response.[12−16] Hence, it is crucial to the development of $Ti_3C_3T_x$-based NH_3 sensors with high sensing performance.

To overcome these shortcomings, the heterojunction construction is considerate as the effective strategy.[17−22] For example, Liu et al. synthesized In_2O_3 and $Ti_3C_2T_x$ composites hydrothermally and achieved enhanced response and ppm-level NH_3 detection. Compared with the pure $Ti_3C_2T_x$, the response to 20 ppm of NH_3 is enhanced by 2677% at RT, in

Received: March 20, 2025
Revised: May 18, 2025
Accepted: May 29, 2025
Published: June 5, 2025

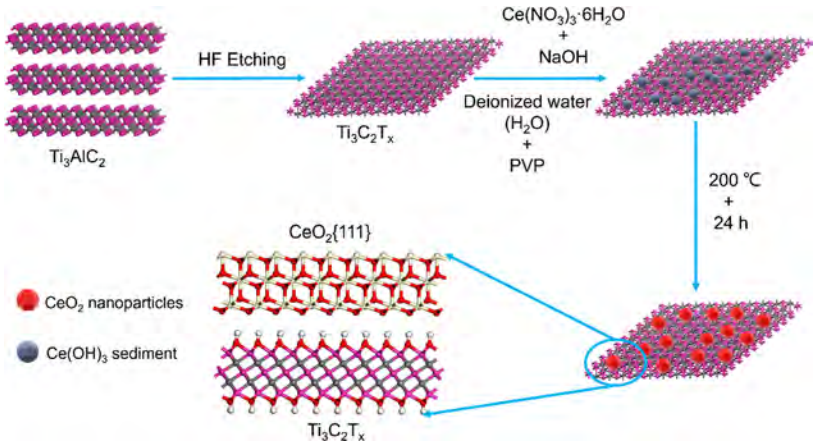

Figure 1. Schematic illustration of the preparation of the $CeO_2/Ti_3C_2T_x$ composite.

addition to response and recovery time of 98 and 580 s, respectively.[17] Song et al. reported the α-Fe_2O_3−$Ti_3C_2T_x$ composite has excellent properties in the detection of NH_3 at RT, such as a recovery time of less than 2.5 s for 5 ppm of NH_3 at RT.[18] Zhou et al. reported that the response of TiO_2 and N-doped $Ti_3C_2T_x$ composite to 200 ppb NH_3 is about 7.3%, together with decent repeatability, stability, and selectivity.[19] In situ synthesis of metal oxide on $Ti_3C_2T_x$ can combine the structural advantages and avoid the agglomeration of $Ti_3C_3T_x$, increasing the active adsorption sites for NH_3 molecular. Meanwhile, the heterojunction in composites could alter the electrical transport and adsorption energy.[17−22] Among the various metal oxides, cerium oxide (CeO_2) has a small oxygen vacancy formation energy.[23−28] Oxygen vacancies in CeO_2 can enhance the adsorption of NH_3 molecules to improve the sensing properties.[23−28] If the $Ti_3C_3T_x$ is decorated with CeO_2 nanoparticles, the sensing performance to NH_3 at RT may be enhanced effectively.

Herein, $Ti_3C_2T_x$ prepared by HF etching is combined with CeO_2 nanoparticles to form the heterojunction. The CeO_2 nanoparticles are anchored on the surface of $Ti_3C_2T_x$ to increase the gas adsorption. Compared to $Ti_3C_2T_x$, the response of CeO_2 and $Ti_3C_2T_x$ composite for 10 ppm of NH_3 is increased by 180% at RT. First-principles calculation is conducted to elucidate the mechanism.

2. EXPERIMENTAL SECTION

2.1. Synthesis of CeO_2 and $Ti_3C_2T_x$ Composites. The $Ti_3C_2T_x$ powders were prepared by etching with hydrofluoric acid (HF). The Ti_3AlC_2 powders were etched to remove Al in the HF solution under stirring at 50 °C for 24 h. The suspension was washed several times using deionized water (DI) until neutral. Then, the obtained $Ti_3C_2T_x$ was transferred to ethanol, and the mixture was stirred at RT for 12 h. The mixed solution was centrifuged and vacuum-dried at 50 °C for 12 h to attain the $Ti_3C_2T_x$ MXene power.[17−19] Afterward, 0.2 g of $Ce(NO)_36H_2O$, 0.05 g of NaOH, and 0.15 g of PVP were decanted into the $Ti_3C_2T_x$ solution and transferred to a Teflon-lined autoclave (50 mL) for reaction at 200 °C for 24 h. Before the hydrothermal reaction, nitrogen gas was continuously flowed into solution to remove the dissolved oxygen. The precipitate was collected by centrifugation, washed with DI water and ethanol six times, and vacuum-dried at 60 °C for 12 h (Figure 1). To study the effects of $Ti_3C_2T_x$ on the gas sensing response of composites, the 0.5 wt %, 1.5 wt %, 2.5 wt %, and 5 wt % of $Ti_3C_2T_x$ (relative to 0.2 g of $Ce(NO)_3·6H_2O$) were added to the solution, and the samples were labeled as Ce−Ti-a, Ce−Ti-b, Ce−Ti-c, and Ce−Ti-d, respectively. The CeO_2 was synthesized by the same method without $Ti_3C_2T_x$ powders.

2.2. Materials Characterization. The crystal structures of CeO_2, $Ti_3C_2T_x$, and $CeO_2/Ti_3C_2T_x$ compounds were determined by X-ray diffraction (XRD, Bruker D8 Advance, Cu Kα1: λ = 0.154056 nm) using a scanning range between 5° and 90° at a rate of 8°/min. The Raman spectra were acquired from the Horiba HR Evolution (514 nm laser). The chemical states were determined by X-ray photoelectron spectroscopy (XPS, Thermo Fisher ESCALAB Xi$^+$). The morphology of CeO_2, $Ti_3C_2T_x$, and $CeO_2/Ti_3C_2T_x$ composites was examined by scanning electron microscopy (FESEM, Zeiss Sigma300) and transmission electron microscopy (TEM, JEM-2100Plus).

2.3. Sensing Assessment. The prepared samples were added to deionized water to form a slurry and then spin-coated on the Au interdigital electrodes. After room-temperature drying for 12 h at RT, the gas sensor was obtained (Figure S1). The gas sensing performance was tested using the static gas test platform (CGS-8 HP system). The ambient temperature was controlled at RT (26 °C). The NH_3 with the corresponding concentration was prepared by injecting the ammonia aqueous solution (25 wt %) into the chamber, and the changes in sensor resistance were monitored during NH_3 exposure. The ethanol (99.7 wt %), acetone (99.5 wt %), and toluene (99.5 wt %) solution were evaporated at 180 °C to attain the ethanol, acetone, and toluene gas. The concentration (C_0, ppm) was calculated by eq 1

$$C_0 = \frac{22.4 \times \rho_o \times C_s \times V_L}{M_0 \times V_C} \quad (1)$$

where the ρ_o is the density of liquid (g/cm^3), C_s is the concentration of liquid (wt %), V_L and V_C are the volume of liquid and chamber (mL), respectively. The M_0 is the molar mass of organics (g/mol). The 500 ppm of H_2S and SO_2 sample gas was injected into test chamber by using a microinjector, and the concentration (C_0, ppm) was calculated by eq 2

$$C_0 = \frac{V_{gas} \times 500}{V_C} \quad (2)$$

where the V_{gas} is the volume of dry gas (mL) and V_C is the volume of chamber (mL). In addition, the response (S_g) is defined as follows eq 3

$$S_g = \frac{R_g - R_a}{R_a} \times 100 \ (R_g > R_a) \quad \text{or}$$
$$S_g = \frac{R_a - R_g}{R_a} \times 100 \ (R_g < R_a) \quad (3)$$

in which R_a and R_g are the resistance values of sensor upon exposed to air and target gas, respectively. The time required to reach 90% of total resistance change during adsorption and desorption is referred to as the response and recovery times, respectively.

2.4. DFT Calculations. The work function, density of states, and adsorption energy were derived by density functional theory

https://doi.org/10.1021/acsanm.5c01721
ACS Appl. Nano Mater. 2025, 8, 12090−12099

calculation. The Perdew–Burke–Ernzerhof functional was selected for the exchange–correlation potential.[29−31] The 450 eV energy cutoff, 0.01 eV Å^{-1} atomic Hellman–Feynman force threshold, and 10^{-4} eV electron self-consistent iteration were used in the calculations. The 3 × 3 × 1 *k*-point grid was used to calculate the heterostructure, and a 20 Å vacuum layer was set to limit self-interactions. The adsorption energy for gas molecules is calculated as follows eq 4

$$E_{ads} = E_{total} - E_{gas} - E_{sub} \quad (4)$$

where E_{total}, E_{gas}, and E_{sub} are the energy of total system, gas molecule, and substrate, respectively.

3. RESULTS AND DISCUSSION

3.1. Materials Characterization. The structures of CeO_2, $Ti_3C_2T_x$, and $CeO_2/Ti_3C_2T_x$ compounds are determined by XRD. As displayed in Figure 2, the peak at about 7.6° stems

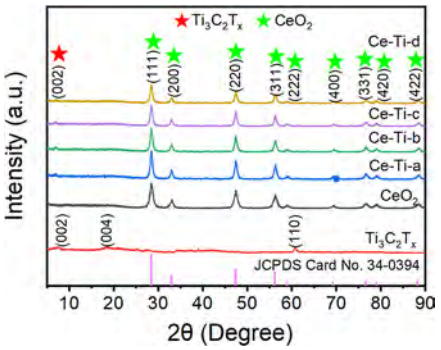

Figure 2. XRD patterns of CeO_2, $Ti_3C_2T_x$, and $CeO_2/Ti_3C_2T_x$ composites.

from the (002) plane of $Ti_3C_2T_x$ and the other peaks correspond to the (111), (200), (220), (311), (222), (400), (331), (420), and (422) planes of CeO_2 (JCPDS card No. 34-0394). The XRD peaks of $Ti_3C_2T_x$ and CeO_2 are detected from $CeO_2/Ti_3C_2T_x$ composites, corroborating the successful fabrication of composites. The Raman scattering spectra of CeO_2, $Ti_3C_2T_x$, and composites are depicted in Figure 3, in

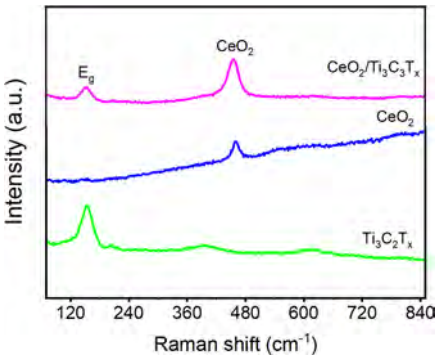

Figure 3. Raman spectra of $Ti_3C_2T_x$, CeO_2, and $CeO_2/Ti_3C_2T_x$ composites (Ce–Ti-b).

which the peak at about 153.47 cm^{-1} arises from $Ti_3C_2T_x$.[20] After incorporation of CeO_2 nanoparticles, a sharp peak appears at about 456.96 cm^{-1}, indicating the presence of CeO_2 in the composite.[32,33] Compared with the pure CeO_2, the Raman peak red-shifts by 7 cm^{-1} as an indication of charge transfer between CeO_2 and $Ti_3C_2T_x$.[32]

As shown in Figure 4a–c, $Ti_3C_2T_x$ has an accordion-like multilayer nanosheet structure. Some granular $Ti_3C_2T_x$ is attached to the structure due to the nonuniformity of the precursor and nanosheets damage during ultrasonic treatment and stirring. Figure 4d–g shows the SEM morphology of CeO_2 and $Ti_3C_2T_x$ composites. There are many CeO_2 nanoparticles on the edge and surface of $Ti_3C_2T_x$ nanosheets, which form a heterointerface and provide abundant adsorption sites, promoting the adsorption of gas molecules. Figure 4h–l shows the SEM elemental maps of composite. The Al concentration decreases resulting from etching, and the Ce elements are distributed on the surface of $Ti_3C_2T_x$, which further confirms that the heterojunction is formed in the composites.

Figure 5 shows the TEM images of CeO_2, $Ti_3C_2T_x$, and $CeO_2/Ti_3C_2T_x$ compounds. As displayed in Figure 5a,b, without $Ti_3C_2T_x$, the pure CeO_2 nanoparticles are reunited, and the size of the CeO_2 nanoparticles is about 24.89 nm. The HR-TEM image in Figure 5c reveals lattice fringes with an interplanar spacing of 0.32 nm, which can be indexed to the (111) plane of CeO_2. The pristine $Ti_3C_2T_x$ exhibits a multilayered structure (Figure 5d,e). The lattice spacing of 0.26 nm corresponds to the (100) plane of $Ti_3C_2T_x$. The selected-area electron diffraction pattern demonstrates the typical hexagonal structure of $Ti_3C_2T_x$ (Figure 5f). The TEM images of $CeO_2/Ti_3C_2T_x$ in Figure 5g,h show that the CeO_2 nanoparticles are distributed on the surface of $Ti_3C_2T_x$, and the size is decreased to 14.32 nm, which indicates that the addition of $Ti_3C_2T_x$ could effectively decrease the size of CeO_2 nanoparticles during preparation, promoting the adsorption of NH_3 molecular. The clear lattice fringes of 0.32 and 0.26 nm match the (111) plane of CeO_2 and the (100) plane of $Ti_3C_2T_x$, respectively (Figure 5i). The above results indicate the successful preparation of CeO_2 and $Ti_3C_2T_x$ hybrids.

To investigate the chemical states and elemental composition, XPS is carried out. The Ce 3d XPS spectra of CeO_2 in Figure 6a show peaks at about 886.54 eV (u') and 904.98 eV (v') belonged to the Ce^{3+} $3d_{5/2}$ and $3d_{3/2}$ orbitals, indicating presence of oxygen vacancies (O_v). The O 1s spectrum in Figure 6b shows that peaks at about 528.76, 530.96, and 532.89 eV are assigned to Ce–O, O_v, and adsorbed oxygen (O_{ads}), respectively. The Ti 2p spectrum of $Ti_3C_2T_x$ in Figure 6c shows that peaks at about 454.83, 458.34, 461.82, and 464.91 eV are associated with Ti–C, C–Ti–OH, Ti_xO_y, and C–Ti–OH. The C–Ti–OH and Ti_xO_y bonds indicate a stoichiometric mismatch of titanium and oxygen. The hydrogen and hydroxyl groups are formed on the surface by etching.[32] The survey spectrum in Figure 6d reveals that $CeO_2/Ti_3C_2T_x$ hybrids contain C, Ti, Ce, and O, which is consistent with the aforementioned elemental maps. The Ti 2p spectrum of composites in Figure 6e shows the binding energies of Ti–C, C–Ti–OH, Ti_xO_y, and C–Ti–OH are located at about the 455.15, 457.86, 461.14, and 464.65 eV, respectively.[32] In Figure 6f,g, the binding energies of Ce 3d (u' and v') and O 1s (Ce–O, O_v, and O_{ads}) are located at about the 885.13, 904.93, 528.38, 531.26, and 533.92 eV, respectively.[26−28] The proportion of O_v is calculated from the integrated peak area as follows

$$[O_v] = \frac{A_{O_v}}{A_{O_v} + A_{O_L} + A_{O_{ads}}} \quad (5)$$

https://doi.org/10.1021/acsanm.5c01721
ACS Appl. Nano Mater. 2025, 8, 12090−12099

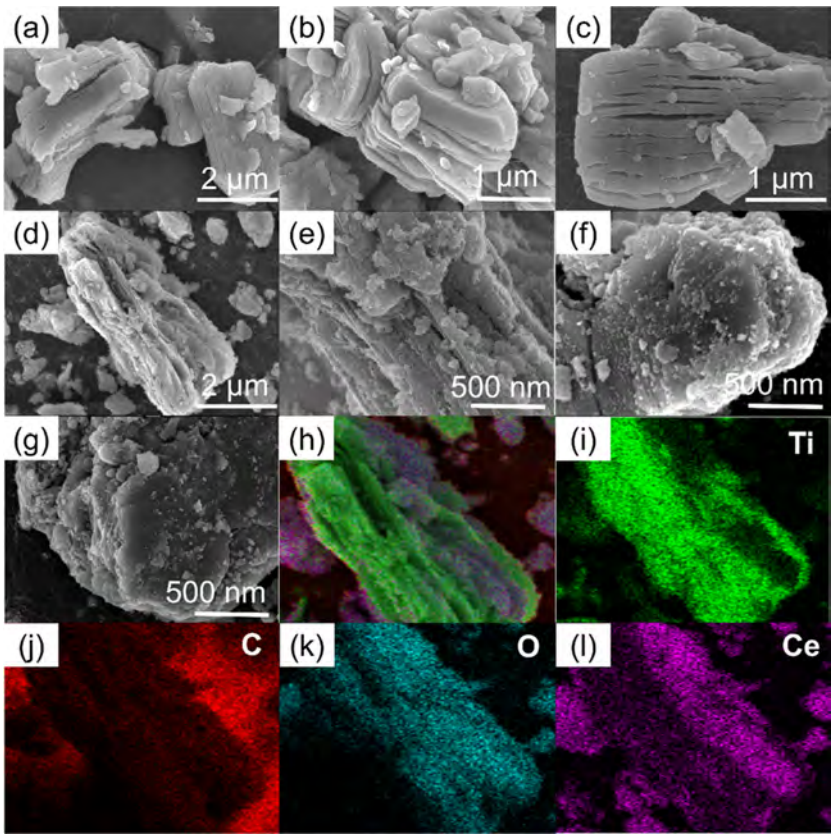

Figure 4. SEM images of (a–c) $Ti_3C_2T_x$, (d–g) $CeO_2/Ti_3C_2T_x$ composites (Ce–Ti-b); SEM elemental maps of the composite: (h) survey, (i) Ti, (j) C, (k) O, and (l) Ce.

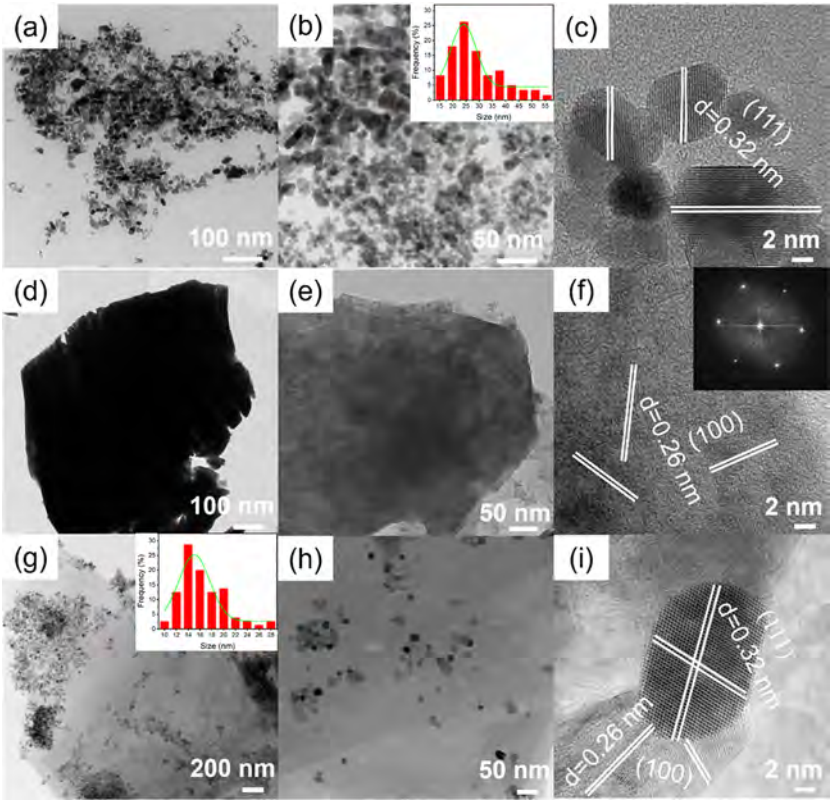

Figure 5. TEM images of (a–c) CeO_2, (d–f) $Ti_3C_2T_x$, and (g–i) $CeO_2/Ti_3C_2T_x$ composites (Ce–Ti-b).

https://doi.org/10.1021/acsanm.5c01721
ACS Appl. Nano Mater. 2025, 8, 12090–12099

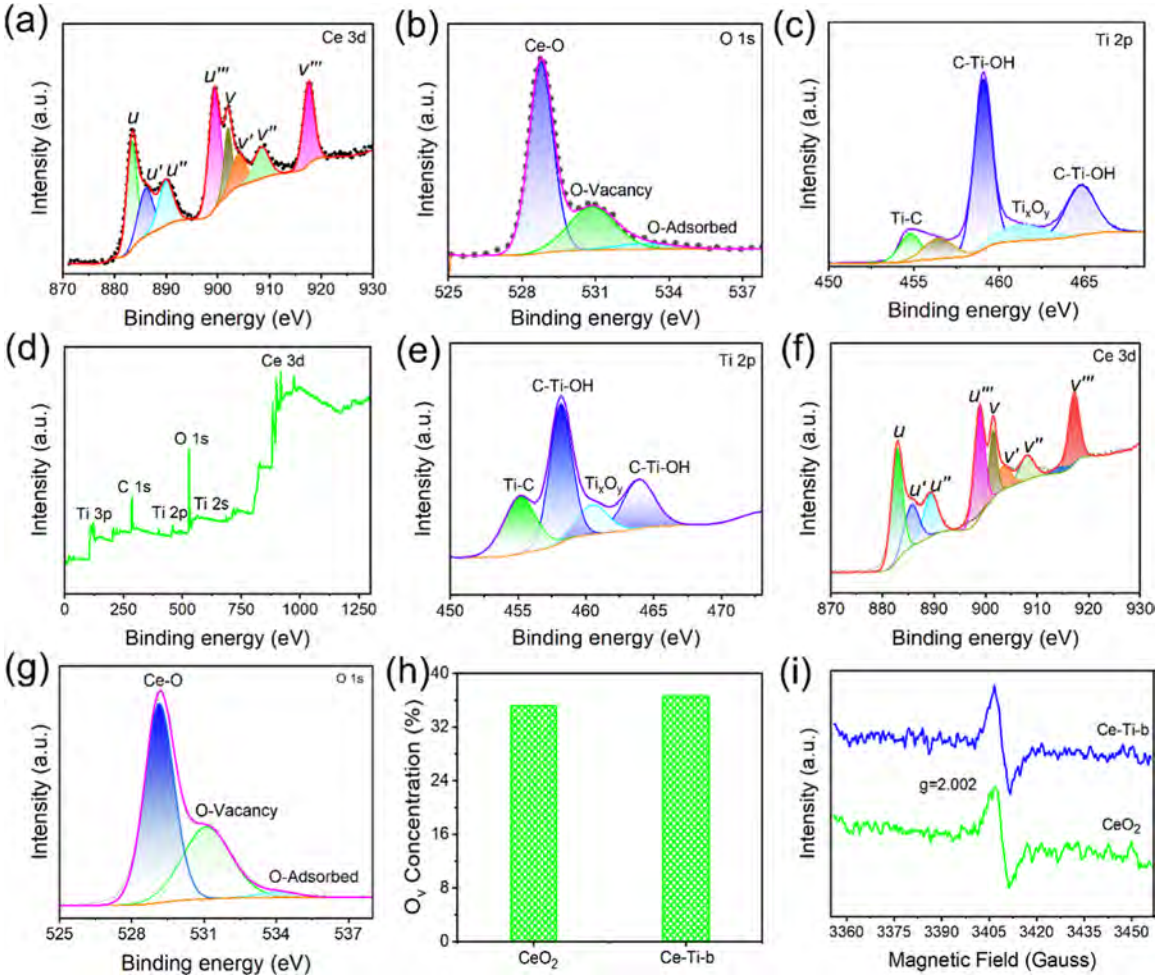

Figure 6. (a) Ce 3d and (b) O 1s XPS spectra of CeO_2. The (c) Ti 2p XPS spectra of $Ti_3C_2T_x$. The (d) survey, (e) Ti 2p, (f) Ce 3d, and (g) O 1s XPS spectra of $CeO_2/Ti_3C_2T_x$ composites (Ce−Ti-b). (h) The O_v concentration of CeO_2 and Ce−Ti-b. The (i) EPR spectra of CeO_2 and Ce−Ti-b.

in which A_{O_v}, A_{O_L}, and $A_{O_{ads}}$ are the integrated area of the XPS peaks of Ce−O, O_v, and O_{ads}, respectively. The O_v concentration of CeO_2 and composites is about 33.15% and 34.62%, respectively, indicating that the density of O_v is increased slightly when the composites are formed (Figure 6h). Additionally, the electron paramagnetic resonance (EPR) of CeO_2 and $CeO_2/Ti_3C_2T_x$ composites is measured and displayed in Figure 6i. The EPR signal at g = 2.002 is clearly observed, which further confirmed that the O_v occurs on the surface of composites. Moreover, a stronger EPR signal means the higher concentration of O_v.[34,35] The composites contain a higher O_v concentration in comparison with CeO_2. Because of lattice constants difference, the stresses are generated at interfaces in composites. It would disrupt the lattice integrity and lower the energy barrier for formation of O_v. Then, the interface region usually has a large number of dislocations and grain boundaries. It would promote oxygen atoms to leave the lattice, resulting in a higher concentration of O_v. In addition, when two different materials contact, electrons are redistributed to balance the Fermi level differences, accelerating the formation of O_v as charge compensation. Hence, the composites contain abundant O_v.

3.2. Sensing Properties. The room-temperature NH_3-sensing performance of CeO_2, $Ti_3C_2T_x$, and $CeO_2/Ti_3C_2T_x$ composites is determined at RT. As displayed in Figure 7a, the resistance (R_a) of CeO_2, $Ti_3C_2T_x$, Ce−Ti-a, Ce−Ti-b, Ce−Ti-c, and Ce−Ti-d is about 136.58 MΩ, 14.61 MΩ, 98.23 MΩ, 65.42 MΩ, 49.36 MΩ, and 41.03 MΩ, respectively. The response of CeO_2 to 10 ppm of NH_3 is about 3.63% at RT, behaving the poor NH_3-sensing response. As for the composite, the response is enhanced when the $Ti_3C_2T_x$ concentration is increased from 0 to 1.5 wt %. However, the response becomes poor when the $Ti_3C_2T_x$ concentration is increased further. Because of the larger band gap, the conductivity of CeO_2 is poor, behaving with the poor NH_3-sensing response. When composited with $Ti_3C_2T_x$, the conductivity is increased and thus the NH_3-sensing response is enhanced because the adsorption ability of $Ti_3C_2T_x$ is lower than that of CeO_2. At high content of $Ti_3C_2T_x$, the adsorption ability of composites for NH_3 would become poor, resulting in a lower NH_3-sensing response. Hence, the composites of CeO_2 and 1.5 wt % $Ti_3C_2T_x$ (Ce−Ti-b) show the highest NH_3-sensing response at RT and are studied further. Figure 7b−d displays the resistance change curves of CeO_2, $Ti_3C_2T_x$, and $CeO_2/Ti_3C_2T_x$ composites (Ce−Ti-b) toward 10 ppm of NH_3 at RT. The response and recovery time of CeO_2 is about 39 and 161 s, respectively. However, the resistance of $Ti_3C_2T_x$ could not restore to the initial resistance, indicating the poor recovery performance. When the composites of CeO_2 and $Ti_3C_2T_x$ are formed, the response and recovery time is about

https://doi.org/10.1021/acsanm.5c01721
ACS Appl. Nano Mater. 2025, 8, 12090−12099

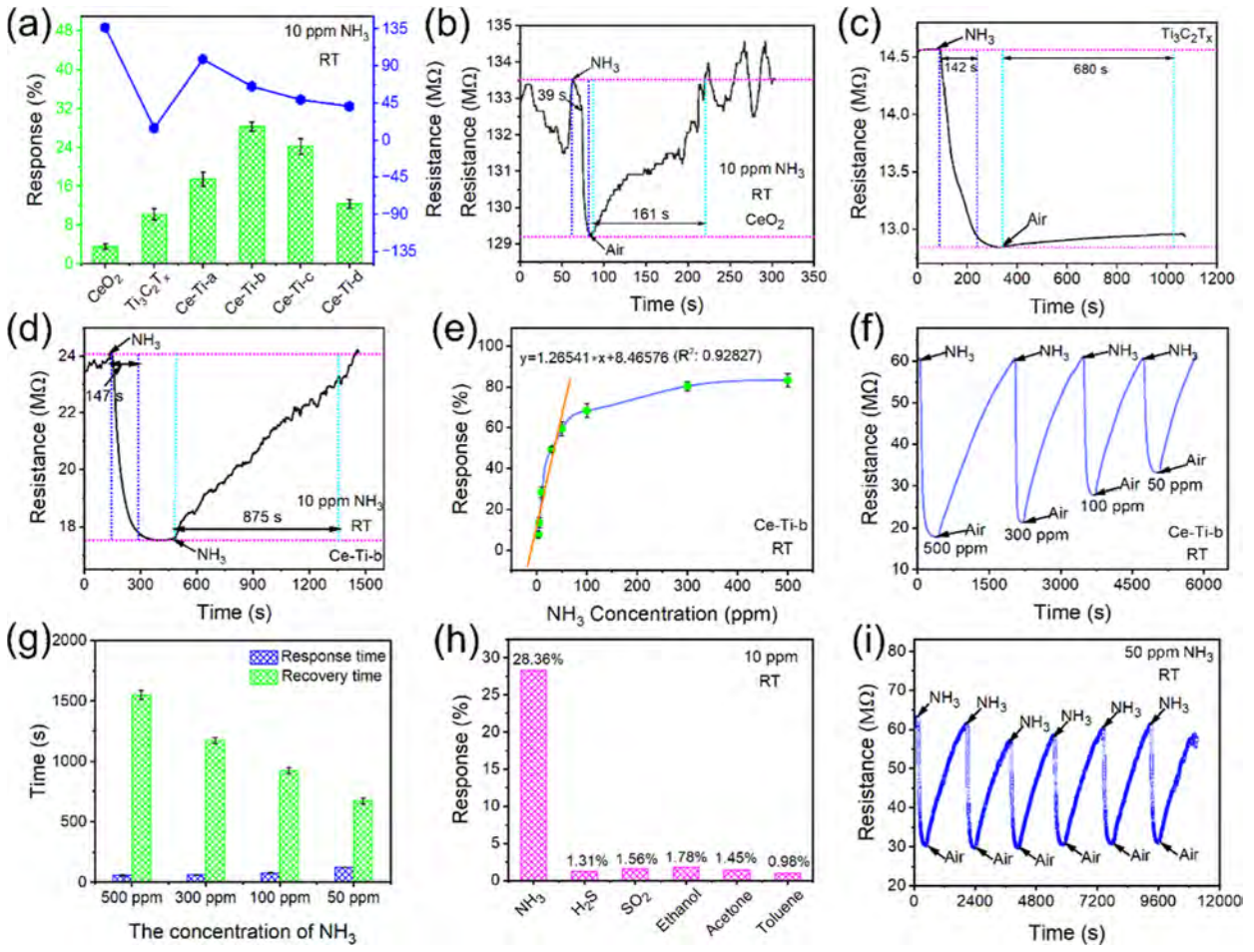

Figure 7. The (a) response and R_a of CeO_2, $Ti_3C_2T_x$, and $CeO_2/Ti_3C_2T_x$ composites to 10 ppm of NH_3 at RT; the response and recovery time of (b) CeO_2, (c) $Ti_3C_2T_x$, and (d) $CeO_2/Ti_3C_2T_x$ (Ce−Ti-b) to 10 ppm of NH_3 at RT; the (e) response value of the Ce−Ti-b sensor to 3−500 ppm of NH_3 at RT; (f) real-time resistance curves of the Ce−Ti-b sensor to 50−500 ppm of NH_3 at RT; the (g) response and recovery time of the Ce−Ti-b sensor to 3−20 ppm of NH_3 at RT; (h) responses of the Ce−Ti-b sensor to different gases at RT; (i) response curves of the Ce−Ti-b sensor to 50 ppm of NH_3 in six cycles.

147 and 875 s, respectively. Hence, fabrication of CeO_2 and $Ti_3C_2T_x$ composites could effectively enhance the NH_3-sensing response and lower recovery time at RT. The corresponding linear fitting curves of response versus NH_3 concentration are displayed in Figure 7e. With an increase of NH_3 concentration from 3 to 500 ppm, the response is enhanced from 7.69% to 83.25%. The response is enhanced by 1.26541% at RT if the NH_3 concentration is increased by 1 ppm at RT in the range of 3−50 ppm. However, the sensing response tends to saturation if the NH_3 concentration is further increased. At high NH_3 concentration, the active sites may be fully occupied by the NH_3 molecular. The charge transfer is nearly independent of NH_3 concentration. Hence, the response reaches the saturation value. Figure 7f displays the real-time sensing response curve of $CeO_2/Ti_3C_2T_x$ hybrids (Ce−Ti-b), showing that the resistance decreases rapidly in NH_3 and then recovers to the initial resistance in air. During the NH_3-sensing response, some highly active adsorption sites would impede the NH_3 molecular desorption, resulting in difficult detaching of all adsorbed NH_3 molecules during the desorption process. In addition, the intermediate products generated during the NH_3-sensing response probably hinder the NH_3 molecular desorption. Hence, the resistance of sensor could not be recovered to initial states completely and the steady state was not achieved during NH_3-sensing response. The response time of Ce−Ti-b to 500, 300, 100, and 50 ppm of NH_3 is about 58 s, 62 s, 78 s, and 125 s, and the recovery time is about 1550 s, 1173 s, 925 s, and 673 s, indicating the excellent response and recovery properties (Figure 7g). At low NH_3 concentration, the reaction rate between NH_3 molecules and adsorbed oxygen molecules is poor. There is enough long time for the sensor's resistance to attain balance. Hence, the response time is longer. With an increase of the NH_3 concentration, the NH_3 molecules diffuse more rapidly to the surface of the sensor, accelerating the adsorption and reaction rates. Hence, the resistance of the sensor could reach balance quickly, showing the lower response time. In addition, with a decrease of NH_3 concentration, the time for the NH_3 molecular desorption is lower, resulting in decreased recovery time. The NH_3-sensing response curves of the Ce−Ti-b sensor toward 10, 1, and 500 ppb are also measured. As displayed in Figure S2, the Ce−Ti-b sensor could achieve a detection of 500 ppb NH_3, which showed the huge application potential in the medical diagnosis of patients. Figure 7h shows the response of the Ce−Ti-b sensor toward 10 ppm of NH_3, H_2S, SO_2, ethanol, acetone, and toluene. The response to NH_3 is much higher than that to H_2S, SO_2, ethanol, acetone, and toluene. Compared with other gas molecular, the adsorption energy of CeO_2 toward NH_3 is much

https://doi.org/10.1021/acsanm.5c01721
ACS Appl. Nano Mater. 2025, 8, 12090−12099

more negative, indicating the higher adsorption ability of the sensor toward NH_3 (Figure S3). Hence, the $CeO_2/Ti_3C_2T_x$ composites show the excellent selectivity toward NH_3 at RT. To test the repeatability performance of the Ce−Ti-b sensor, the six continue response−recover cycles were measured. As displayed in Figure 7i, the relative standard deviation (RSD) of six cycles responses is about 3.27%, behaving with excellent repeatability. To demonstrate the long-term stability of the sensor, the sensor is stored in a normal indoor environment for 15 days. The RSD of response to 50 ppm of NH_3 is about 8.39%, and the response is reduced by only 16.67% after 15 days, showing decent stability (Figure S4). In addition, the EPR spectra of CeO_2 and $Ti_3C_2T_x$ composites were measured before and after 15 days. It is clearly found the EPR signal of composites becomes poor after 15 days, which indicates that the concentration of O_v is reduced after 15 days (Figure S5). Hence, the room-temperature response of the composites toward NH_3 after 15 days becomes poor.

The influence of working temperature on the 10 ppm of NH_3-sensing response is studied. As shown in Figure S6a, the response is reduced by 0.2% if the working temperature is increased by 1 °C, which is equivalent to a decrease of 158 ppb NH_3 at RT. Higher thermal activation could promote the desorption ability of NH_3 molecules. No enough long time for the sensor to react with NH_3 molecules, resulting in the lower sensing response.[36−38] The influence of environmental humidity (RH) on the 10 ppm of NH_3-sensing response is also studied. The environmental humidity was controlled through injecting deionized water onto an evaporator with heating temperature of 180 °C by a microsyring. With an increase of environmental humidity, the response declines (Figure S6b). Figure S6c,d displays the NH_3-sensing response curve of CeO_2 and $Ti_3C_2T_x$ compounds under dry air and 87% RH by using a dynamic gas sensing test system. In dry air, the resistance is reduced obviously when exposed to NH_3 and then the resistance is completely recovered to the initial resistance. The room-temperature sensing response to 500, 300, and 100 ppm of NH_3 is about 89.5%, 75%, and 69.36%, respectively. However, at high humidity (87% RH), the response to 500, 300, and 100 ppm of NH_3 is reduced to 22.26%, 16.23%, and 9.38%, respectively, and the resistance could not be recovered to the initial value, showing the poor recovery performance. At higher humidity, the water molecules are adsorbed on the surface of the sensor, which forms H_3O^+ molecules layers. The layer of H_3O^+ molecules prevents charge transfer between them, resulting in decrease of sensing response.[39−41] In addition, the comparison of the sensing performance of $CeO_2/Ti_3C_2T_x$ composites in this work with other previous work is presented in Table S1. The pure $Ti_3C_2T_x$ shows the lower NH_3-sensing response, longer response, and recovery time at RT.[12,14,15,41,42] When composited with ZnO,[43] CuO,[44] and TiO_2,[45,46] the NH_3-sensing response is enhanced. However, it is still lower than that of CeO_2 and $Ti_3C_2T_x$ composites in this work. In addition, the $CeO_2/Ti_3C_2T_x$ composites also have excellent response and recovery rate. Hence, fabrication of CeO_2 and $Ti_3C_2T_x$ composites in this work displays the excellent NH_3-sensing response at RT.

3.3. Sensing Mechanism. The enhanced sensing properties arise from the strong adsorption of CeO_2, the larger surface area (SA) of $Ti_3C_2T_x$, and heterojunctions. In the first-principles calculations of Figure S7, CeO_2 shows the stronger adsorption ability to NH_3 than $Ti_3C_2T_x$. Although the adsorption energy of CeO_2 for NH_3 is more negative than that of $Ti_3C_2T_x$, the response of pristine $Ti_3C_2T_x$ to 10 ppm of NH_3 is higher than that of CeO_2 at RT. In fact, besides adsorption energy, the sensing response is also depended on the morphology and electrical conductivity. The multilayer structure, abundant exposed edges, and high carrier mobility of $Ti_3C_2T_x$ give rise to ample adsorption sites for NH_3 molecules and enhanced NH_3 adsorption and diffusion. According to the results of nitrogen adsorption−desorption experiments, the Brunauer−Emmett−Teller (BET) SA of CeO_2 is about 73.1152 m^2/g (Figure S8a). When composited with $Ti_3C_2T_x$, the BET SA increased to 77.0326 m^2/g (Figure S8b). Hence, when the composites of $Ti_3C_2T_x$ and CeO_2 are formed, the CeO_2 nanoparticles covered the surface and interlayers of multilayered $Ti_3C_2T_x$ nanosheets and the specific SA is increased. Furthermore, the adsorption energy of the composites is much more negative than that of pure CeO_2 and $Ti_3C_2T_x$. Fabrication of composites promotes the adsorption ability of NH_3 molecular and thus enhances the NH_3-sensing response (Figure 8a,b).

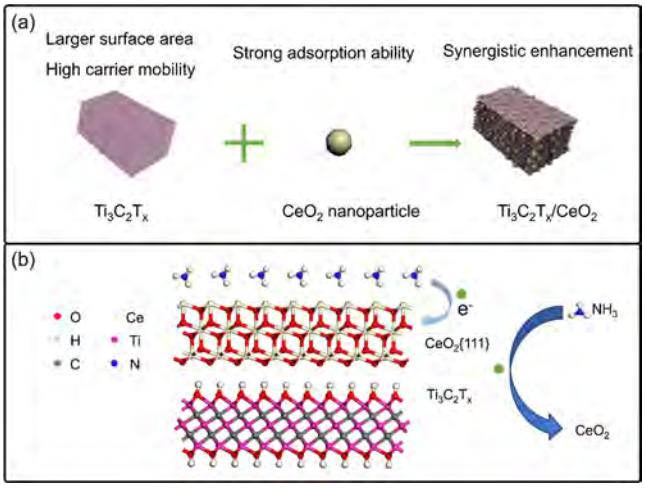

Figure 8. (a) Schematic illustration of the sensing mechanism of CeO_2 and $Ti_3C_2T_x$ composites and (b) schematic diagram of NH_3 adsorption.

To reveal the role of chemically adsorbed oxygen (O_2^-) on NH_3-sensing response, the room-temperature response of the Ce−Ti-b sensor to 100 ppm of NH_3 in N_2, air, and O_2 is measured, respectively. As shown in Figure S9, the response of composites toward 100 ppm of NH_3 in O_2 is higher than that in N_2. In N_2, almost no O_2 is adsorbed on the surface. The NH_3 molecules could not react with O_2^- ions and directly release electrons to sensors, resulting in decreased resistance. In O_2, lots of O_2 molecules are adsorbed on the surface, and the response is enhanced. It confirms that the NH_3 molecules could react with O_2^- ions, and more electrons are produced on the surface of the sensor (eqs 6−8).[43−46]

$$O_2\ (gas) \rightarrow O_2\ (ads) \quad (6)$$

$$O_2\ (ads) + e^- \rightarrow O_2^- \quad (7)$$

$$4NH_3 + O_2^- \rightarrow 4NO + 6H_2O + 5e^- \quad (8)$$

To reveal the role of heterojunctions on the sensing properties, the work functions of $Ti_3C_2T_x$ and CeO_2 are calculated and the results are displayed in Figure S10a,b. The work function of $Ti_3C_2T_x$ is 4.27 eV, which is smaller than that

https://doi.org/10.1021/acsanm.5c01721
ACS Appl. Nano Mater. 2025, 8, 12090−12099

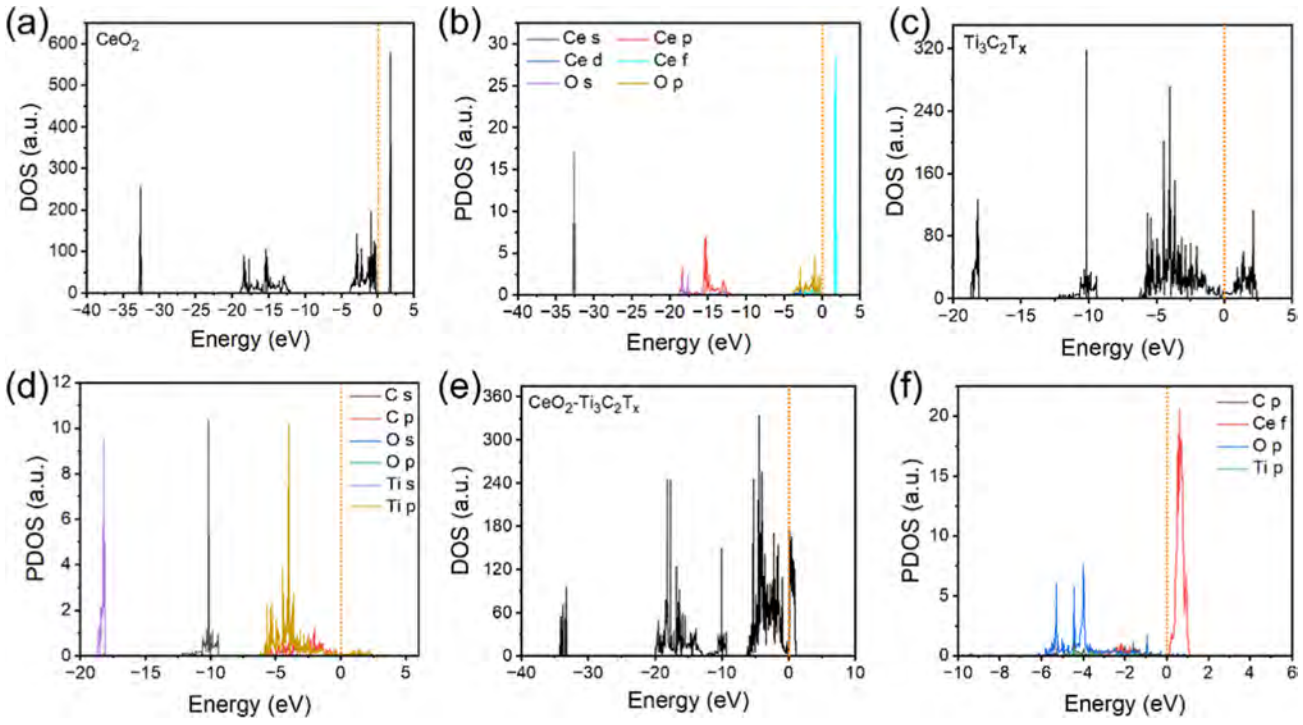

Figure 9. DOS and PDOS of (a,b) CeO_2, (c,d) $Ti_3C_2T_x$, and (e,f) $CeO_2/Ti_3C_2T_x$ heterojunction.

of CeO_2 (6.03 eV). When CeO_2 and $Ti_3C_2T_x$ contacts, free electrons move from $Ti_3C_2T_x$ to CeO_2 until the Fermi levels of two materials reach a balance, consequently forming a heterojunction at the interface (Figure S10c,d). The contact resistance (R_c) is expressed by the following eq 9:[13]

$$R_c \propto \frac{1}{n} e^{\varphi_B/kT} \tag{9}$$

where n is the electron concentration, φ_B is the interface barrier height of heterojunction, k is Boltzmann's constant, and T is the absolute temperature. In air, the oxygen molecule is mainly adsorbed on the surface of composites and captures electrons to form O_2^-. The adsorbed O_2^- ions broaden the space charge region (Figure S10e). Upon exposure to NH_3, the NH_3 molecule is mainly adsorbed on the surface of CeO_2, releasing the electrons to CeO_2. The electron concentration is increased. At the same time, the Fermi level of CeO_2 is upshifted. The difference of the work function between CeO_2 and $Ti_3C_2T_x$ is reduced, resulting in a decreased space charge region and φ_B. Correspondingly, the R_c decreases, making electron transfer at the interface easier and enhancing room-temperature NH_3-sensing response (Figure S10f). Except for the heterojunction, O_v also plays the important role in enhancing NH_3-sensing response. Based on XPS and EPR results, the composites possess a higher density of O_v than CeO_2. The abundant O_v provides more active sorption sites and electrons to interact with NH_3 molecules, further facilitating the gas−solid reactions.

In addition, the DOS and PDOS of CeO_2, $Ti_3C_2T_x$, and the $CeO_2/Ti_3C_2T_x$ composites are calculated. As shown in Figure 9a,b, the conduction band (CB) and valence band (VB) of CeO_2 are mainly associated with Ce 4f and O 2p, respectively, with a band gap of about 2.43 eV. Electrons are difficult to transfer from VB to CB, resulting in poor conductivity. With regard to $Ti_3C_2T_x$, the VB and CB overlap at the Fermi level, showing metallic properties. The CB and VB arise mainly from Ti 2p and C 2p, respectively (Figure 9c,d). As for the heterojunction of $CeO_2/Ti_3C_2T_x$, the Fermi level is close to CB, making it n-type, and CB and VB are primarily associated with C 2p and Ce 4f, respectively (Figure 9e,f). The band gap is about 0.23 eV, and electrons can move from VB to CB easily, thus giving rise to excellent conductivity. The results reveal that $CeO_2/Ti_3C_2T_x$ hybrids have better sensing properties for ammonia at RT, boding well for commercial adoption.

4. CONCLUSION

The $CeO_2/Ti_3C_2T_x$ heterojunction is designed and fabricated to enhance the NH_3-sensing performance. Compared with $Ti_3C_2T_x$, the response of $CeO_2/Ti_3C_2T_x$ for 10 ppm of NH_3 at RT increases by 180%, together with the fast response and recovery rate. The composite also has excellent reversibility and selectivity. According to DFT calculations, the adsorption energy of CeO_2 toward NH_3 is more negative than that of $Ti_3C_2T_x$. The CeO_2 nanoparticles in the composites form active adsorption sites. The band gap of CeO_2 is about 2.43 eV. When combined with $Ti_3C_2T_x$, the band gap decreases to 0.35 eV, thus enabling electrons to move from VB to CB easily for better conductivity. Furthermore, the heterojunction formed at the interface prolongs the carrier lifetime, consequently promoting charge transfer and response to NH_3.

■ ASSOCIATED CONTENT

Supporting Information

The Supporting Information is available free of charge at https://pubs.acs.org/doi/10.1021/acsanm.5c01721.

Photograph of the gas sensor; long stability of the sensor; EPR curves of CeO_2 and $Ti_3C_2T_x$ composites; response of sensors at different temperatures, humidity, and background gas; adsorption energy of NH_3 molecules on the surface of CeO_2, $Ti_3C_2T_x$, and $CeO_2/Ti_3C_2T_x$ composites; BET SA of CeO_2 and

https://doi.org/10.1021/acsanm.5c01721
ACS Appl. Nano Mater. 2025, 8, 12090−12099

$CeO_2/Ti_3C_2T_x$ composites; work function of $Ti_3C_2T_x$ and CeO_2; and comparison of NH_3-sensing performance in this work with those in previous work (PDF)

AUTHOR INFORMATION

Corresponding Authors

Lizhai Zhang − *School of Materials Science and Engineering, Shaanxi University of Technology, Hanzhong 723001 Shaanxi, China; State Key Laboratory for Mechanical Behavior of Materials, Xi'an Jiaotong University, Xi'an 710049 Shaanxi, China; Department of Physics, Department of Materials Science and Engineering, and Department of Biomedical Engineering, City University of Hong Kong, Kowloon 999077 Hong Kong, China;* orcid.org/0000-0002-6474-9518; Email: zhanglizhai0512@snut.edu.cn

Taotao Ai − *School of Materials Science and Engineering, Shaanxi University of Technology, Hanzhong 723001 Shaanxi, China;* orcid.org/0000-0002-5795-5751; Email: aitaotao0116@126.com

Paul K. Chu − *Department of Physics, Department of Materials Science and Engineering, and Department of Biomedical Engineering, City University of Hong Kong, Kowloon 999077 Hong Kong, China;* orcid.org/0000-0002-5581-4883; Email: paul.chu@cityu.edu.hk

Authors

Jiayuan Xu − *Natural Active Industrialization Engineering Technology Research Centre of Shaanxi Province, Shaanxi University of Technology, Hanzhong 723001 Shaanxi, China;* orcid.org/0009-0008-3874-1900

Dingyuan Wang − *School of Materials Science and Engineering, Shaanxi University of Technology, Hanzhong 723001 Shaanxi, China;* orcid.org/0009-0007-0425-9457

Xinyu Lei − *School of Materials Science and Engineering, Shaanxi University of Technology, Hanzhong 723001 Shaanxi, China;* orcid.org/0009-0001-7494-0818

Henghui Sun − *School of Materials Science and Engineering, Shaanxi University of Technology, Hanzhong 723001 Shaanxi, China;* orcid.org/0000-0001-5180-9836

Yuhong Huang − *College of Physics and Information Technology, Shaanxi Normal University, Xi'an 710062 Shaanxi, China*

Fei Ma − *State Key Laboratory for Mechanical Behavior of Materials, Xi'an Jiaotong University, Xi'an 710049 Shaanxi, China;* orcid.org/0000-0002-3911-7121

Complete contact information is available at: https://pubs.acs.org/10.1021/acsanm.5c01721

Author Contributions

The manuscript was written through contributions of all authors. All authors have given approval to the final version of the manuscript.

Notes

The authors declare no competing financial interest.

ACKNOWLEDGMENTS

This work was jointly supported by the Natural Science Foundation of Shaanxi Province (2023-JC-QN-0476), the Shaanxi University of Technology Research Grant (no. SLGRCQD2207), the Scientific research project of Shaanxi Provincial Education Department (no. 23JK0375), the Science and technology program for overseas students of Shaanxi province (2023016), and the City University of Hong Kong Donation Research Grants (DON-RMG no.9229021 and 9220061).

REFERENCES

(1) Yamulki, S.; Harrison, R. M.; Goulding, K. W. T. Ammonia surface-exchange above an agricultural field in Southeast England. *Atmos. Environ.* **1996**, *30*, 109−118.

(2) Sutton, M. A.; Erisman, J. W.; Dentener, F.; Möller, D. Ammonia in the environment: From ancient times to the present. *Environ. Pollut.* **2008**, *156*, 583−604.

(3) Kwak, D.; Lei, Y.; Maric, R. Ammonia gas sensors: a comprehensive review. *Talanta* **2019**, *204*, 713−730.

(4) Apsimon, H. M.; Barker, B. M.; Kayin, S. Modelling studies of the atmospheric release and transport of ammonia in anticyclonic episodes. *Atmos. Environ.* **1994**, *28*, 665−678.

(5) Chaudhary, V.; Ashraf, N.; Khalid, M.; Walvekar, R.; Yang, Y.; Kaushik, A.; Mishra, Y. K. Emergence of MXene−Polymer Hybrid Nanocomposites as High-Performance Next-Generation Chemiresistors for Efficient Air Quality Monitoring. *Adv. Funct. Mater.* **2022**, *32*, 2112913.

(6) Singh, S.; Deb, J.; Sarkar, U.; Sharma, S. MoS_2/WO_3 Nanosheets for Detection of Ammonia. *ACS Appl. Nano Mater.* **2021**, *4*, 2594−2605.

(7) Beniwal, A.; Ganguly, P.; Khandelwal, G.; Gond, R.; Rawat, B.; Li, C. Additive Strategies to Mitigate Humidity Interference Effects on PEDOT:PSS Sensors for Ammonia Detection. *IEEE Sens. J.* **2025**, *25*, 9357−9366.

(8) Gond, R.; Shukla, P.; Prakash, B.; Rawat, B. Vertically Aligned MoS_2/ZnO Heterostructure for Highly Selective NH_3 Sensing at Room Temperature. *ACS Appl. Electron. Mater.* **2024**, *6*, 2728−2738.

(9) Bai, J. Z.; Shen, Y. B.; Zhao, S. K.; Chen, Y. S.; Li, G. D.; Han, C.; Wei, D. Z.; Yuan, Z. Y.; Meng, F. L. Flower-like MoS_2 hierarchical architectures assembled by 2D nanosheets sensitized with SnO_2 quantum dots for high-performance NH_3 sensing at room temperature. *Sens. Actuators, B* **2022**, *353*, 131191.

(10) Beniwal, A.; Gond, R.; Karagiorgis, X.; Rawat, B.; Li, C. Room-Temperature-Operated Fe_2O_3/PANI-Based Flexible and Eco-Friendly Ammonia Sensor With Sub-ppm Detectability. *IEEE Sens. Lett.* **2025**, *9*, 1−4.

(11) Wang, W. X.; Zhen, Y. H.; Zhang, J. Y.; Li, Y. D.; Zhong, H.; Jia, Z. L.; Xiong, Y.; Xue, Q. Z.; Yan, Y. G.; Alharbi, N. S.; Hayat, T. SnO_2 nanoparticles-modified 3D-multilayer MoS_2 nanosheets for ammonia gas sensing at room temperature. *Sens. Actuators, B* **2020**, *321*, 128471.

(12) Lee, E.; VahidMohammadi, A.; Prorok, B. C.; Yoon, Y. S.; Beidaghi, M.; Kim, D. J. Room temperature gas sensing of two-dimensional titanium carbide (MXene). *ACS Appl. Mater. Interfaces* **2017**, *9*, 37184−37190.

(13) You, C. W.; Fu, T.; Li, C. B.; Song, X.; Tang, B.; Song, X.; Yang, Y.; Deng, Z. P.; Wang, Y. Z.; Song, F. A Latent-Fire-Detecting Olfactory System Enabled by Ultra-Fast and Sub-ppm Ammonia-Responsive $Ti_3C_2T_x$ MXene/MoS_2 Sensors. *Adv. Funct. Mater.* **2022**, *32*, 2208131.

(14) Wu, M.; He, M.; Hu, Q. K.; Wu, Q. H.; Sun, G.; Xie, L. L.; Zhang, Z. Y.; Zhu, Z. G.; Zhou, A. G. Ti_3C_2 MXene-Based Sensors with High Selectivity for NH_3 Detection at Room Temperature. *ACS Sens.* **2019**, *4*, 2763−2770.

(15) Yang, Z. J.; Liu, A.; Wang, C. L.; Liu, F. M.; He, J. M.; Li, S. Q.; Wang, J.; You, R.; Yan, X.; Sun, P.; Duan, Y.; Lu, G. Y. Improvement of gas and humidity sensing properties of organ-like MXene by alkaline treatment. *ACS Sens.* **2019**, *4*, 1261−1269.

(16) Zhao, Q. N.; Zhou, W. Z.; Zhang, M. X.; Wang, Y.; Duan, Z. H.; Tan, C. L.; Liu, B. H.; Ouyang, F. P.; Yuan, Z.; Tai, H. L.; Jiang, Y. D. Edge-Enriched $Mo_2TiC_2T_x$/MoS_2 Heterostructure with Coupling Interface for Selective NO_2 Monitoring. *Adv. Funct. Mater.* **2022**, *32*, 2203528.

(17) Liu, Z.; He, T. T.; Sun, H. Y.; Huang, B. Y.; Li, X. G. Layered MXene heterostructured with In_2O_3 nanoparticles for ammonia sensors at room temperature. *Sens. Actuators, B* **2022**, *365*, 131918.
(18) Liu, M.; Ji, J.; Song, P.; Wang, J. X.; Wang, Q. Sensing performance of α-Fe_2O_3/$Ti_3C_2T_x$ MXene nanocomposites to NH_3 at room temperature. *J. Alloys Compd.* **2022**, *898*, 162812.
(19) Zhou, Y.; Wang, Y. H.; Wang, Y. J.; Yu, H. C.; Zhang, R. J.; Li, J.; Zang, Z. G.; Li, X. MXene $Ti_3C_2T_x$-Derived Nitrogen-Functionalized Heterophase TiO_2 Homojunctions for Room-Temperature Trace Ammonia Gas Sensing. *ACS Appl. Mater. Interfaces* **2021**, *13*, 56485−56497.
(20) Zhao, H. C.; Li, J.; She, X. P.; Chen, Y.; Wang, M. Q.; Wang, Y. J.; Du, A. J.; Tang, C.; Zou, C.; Zhou, Y. Oxygen vacancy-rich bimetallic Au@Pt core−shell nanosphere functionalized electrospun $ZnFe_2O_4$ nanofibers for chemiresistive breath acetone detection. *ACS Sens.* **2024**, *9*, 2183−2193.
(21) Yu, C. Y.; Liu, J. H.; Zhao, H. C.; Wang, M. Q.; Li, J.; She, X. P.; Chen, Y.; Wang, Y. J.; Liu, B. C.; Zou, C.; He, Y.; Zhou, Y. Sensitive Breath Acetone Detection Based on α-Fe_2O_3 Nanoparticles Modified WO_3 Nanoplate Heterojunctions. *IEEE Trans. Instrum. Meas.* **2024**, *73*, 1−8.
(22) Sun, M. J.; Ding, K.; Lu, Y. J.; She, X. P.; Chen, Y.; Wang, M. Q.; Zou, C.; Liu, X. Y.; Zhou, Y. Two-dimensional p-n heterojunctions of black phosphorus nanosheet-sensitized α-MoO_3 nanoflake for low-temperature chemiresistive NH_3 recognition. *Microchem. J.* **2024**, *207*, 111911.
(23) Wang, Z. M.; Yu, R. B. Hollow micro/nanostructured ceria-based materials: Synthetic strategies and versatile applications. *Adv. Mater.* **2019**, *31*, 1800592.
(24) Michel, C. R.; Martínez-Preciado, A. H. CO sensor based on thick films of 3D hierarchical CeO_2 architectures. *Sens. Actuators, B* **2014**, *197*, 177−184.
(25) Izu, N.; Shin, W.; Matsubara, I.; Murayama, N. Influence of SO_2 gas on output of resistive oxygen sensors using CeO_2 and $Ce_{0.8}Zr_{0.2}O_2$. *J. Electrochem. Soc.* **2005**, *152*, H111.
(26) Niu, J. S.; Liu, I. P.; Chen, K. H.; Tsai, J. H.; Hsu, W. C.; Liu, W. C. Ammonia sensing characteristics of a cerium oxide thin film coated with platinum nanoparticles. *Sens. Actuators, B* **2022**, *369*, 132241.
(27) Liu, C. H.; Tai, H. L.; Zhang, P.; Yuan, Z.; Du, X. S.; Xie, G. Z.; Jiang, Y. D. A high-performance flexible gas sensor based on self-assembled PANI-CeO_2 nanocomposite thin film for trace-level NH_3 detection at room temperature. *Sens. Actuators, B* **2018**, *261*, 587−597.
(28) Li, P. P.; Wang, B.; Qin, C.; Han, C.; Sun, L.; Wang, Y. D. Band-gap-tunable CeO_2 nanoparticles for room-temperature NH_3 gas sensors. *Ceram. Int.* **2020**, *46*, 19232−19240.
(29) Kresse, G.; Furthmüller, J. Efficient iterative schemes for ab initio total-energy calculations using a plane-wave basis set. *Phys. Rev. B* **1996**, *54*, 11169−11186.
(30) Kresse, G.; Furthmüller, J. Efficiency of Ab initio total energy calculations for metals and semiconductors using a plane-wave basis set. *Comput. Mater. Sci.* **1996**, *6*, 15−50.
(31) Perdew, J. P.; Burke, K.; Ernzerhof, M. Generalized gradient approximation made simple. *Phys. Rev. Lett.* **1996**, *77*, 3865−3868.
(32) Kim, S.; Shin, H.; Lee, J.; Park, C.; Ahn, Y.; Cho, H. J.; Yuk, S.; Kim, J.; Lee, D.; Kim, I. D. Three-Dimensional MoS_2/MXene Heterostructure Aerogel for Chemical Gas Sensors with Superior Sensitivity and Stability. *ACS Nano* **2023**, *17*, 19387−19397.
(33) Kosacki, I.; Suzuki, T.; Anderson, H. U.; Colomban, P. Raman scattering and lattice defects in nanocrystalline CeO_2 thin films. *Solid State Ionics* **2002**, *149*, 99−105.
(34) Wang, L.; Luan, Q. F.; Yang, D.; Yao, X.; Zhou, K. B. Strong electron-conjugation interaction facilitates electron transfer of hemoglobin by $Ce(OH)_3$ nanorods. *RSC Adv.* **2013**, *3*, 6339.
(35) Zhang, L. Z.; Fang, Q. L.; Huang, Y. H.; Xu, K. W.; Chu, P. K.; Ma, F. Oxygen Vacancy Enhanced Gas-Sensing Performance of CeO_2/Graphene Heterostructure at Room Temperature. *Anal. Chem.* **2018**, *90*, 9821−9829.
(36) Liu, M.; Wang, Z. Y.; Song, P.; Yang, Z. X.; Wang, Q. Flexible MXene/RGO/CuO Hybrid Aerogels for High Performance Acetone Sensing at Room Temperature. *Sens. Actuators, B* **2021**, *340*, 129946.
(37) Li, X.; Xu, J. L.; Jiang, Y. D.; He, Z. Z.; Liu, B. H.; Xie, H. K.; Li, H.; Li, Z. M.; Wang, Y.; Tai, H. L. Toward Agricultural Ammonia Volatilization Monitoring: A Flexible Polyaniline/$Ti_3C_2T_x$ Hybrid Sensitive Films Based Gas Sensor. *Sens. Actuators, B* **2020**, *316*, 128144.
(38) Wang, S.; Jiang, Y. D.; Liu, B. H.; Duan, Z. H.; Pan, H.; Yuan, Z.; Xie, G. Z.; Wang, J. B.; Fang, Z.; Tai, H. L. Ultrathin Nb_2CT_x Nanosheets-Supported Polyaniline Nanocomposite: Enabling Ultrasensitive NH_3 Detection. *Sens. Actuators, B* **2021**, *343*, 130069.
(39) Guo, C. Y.; Dong, X.; Zhang, X. F.; Cheng, X. L.; Li, Q.; Sun, Y. J.; Liu, W.; Huo, L. H.; Xu, Y. M. Controllable Construction of Ho_2O_3 nanomaterials with Different Dimensions (1D, 2D, and 3D) for Real-Time Monitoring Human Breathing and Body Surface Humidity Detection. *J. Mater. Chem. A* **2021**, *9*, 11632−11640.
(40) Yu, H. X.; Guo, C. Y.; Zhang, X. F.; Cheng, X. L.; Xu, Y. M.; Gao, S.; Huo, L. H. Tailoring Oxygen Vacancy of Co_3O_4 Microcubes by Annealing $Co_3[Co(CN)_6]_2$ Template in Air for Ultrasensitive Humidity Mapping. *Small Struct.* **2022**, *3*, 2270007.
(41) Kim, S. J.; Koh, H. J.; Ren, C. E.; Kwon, O.; Maleski, K.; Cho, S. Y.; Anasori, B.; Kim, C. K.; Choi, Y. K.; Kim, J.; Gogotsi, Y.; Jung, H. T. Metallic $Ti_3C_2T_x$ MXene Gas Sensors with Ultrahigh Signal-to-Noise Ratio. *ACS Nano* **2018**, *12*, 986−993.
(42) Yuan, W. J.; Yang, K.; Peng, H. F.; Li, F.; Yin, F. X. A flexible VOCs sensor based on a 3D Mxene framework with a high sensing performance. *J. Mater. Chem.* **2018**, *6*, 18116−18124.
(43) Yang, Z. J.; Jiang, L.; Wang, J.; Liu, F. M.; He, J. M.; Liu, A.; Lv, S. Y.; You, R.; Yan, X.; Sun, P.; Wang, C. G.; Duan, Y.; Lu, G. Y. Flexible Resistive NO_2 Gas Sensor of Three-Dimensional Crumpled MXene $Ti_3C_2T_x$/ZnO Spheres for Room Temperature Application. *Sens. Actuators, B* **2021**, *326* (No), 128828.
(44) Wang, D. Y.; Zhang, D. Z.; Yang, Y.; Mi, Q.; Zhang, J. H.; Yu, L. D. Multifunctional Latex/Polytetrafluoroethylene-Based Triboelectric Nanogenerator for Self-Powered Organ-like MXene/Metal−Organic Framework-Derived CuO Nanohybrid Ammonia Sensor. *ACS Nano* **2021**, *15*, 2911−2919.
(45) Tai, H. L.; Duan, Z. H.; He, Z. Z.; Li, X.; Xu, J. L.; Liu, B. H.; Jiang, Y. D. Enhanced ammonia response of $Ti_3C_2T_x$ nanosheets supported by TiO_2 nanoparticles at room temperature. *Sensor. Actuator. B-Chem.* **2019**, *298*, 126874.
(46) Dogra, N.; Gasso, S.; Sharma, A.; Sharma, K. K.; Sharma, S. TiO_2 decorated MXene nanosheets for high-performance ammonia gas sensing at room-temperature. *Surf. Interfaces* **2024**, *48*, 104290.

https://doi.org/10.1021/acsanm.5c01721
ACS Appl. Nano Mater. 2025, 8, 12090−12099

Supporting Information

Enhanced Room-Temperature NH_3-Sensing Performance of $Ti_3C_2T_x$ MXene Decorated with CeO_2 Nanoparticles

Lizhai Zhang[a,b,c], Jiayuan Xu[d], Dingyuan Wang[a], Xinyu Lei[a], Henghui Sun[a], Yuhong Huang [e], Fei Ma [b], Taotao Ai [a*], Paul K Chu [c*]*

[a]School of Materials Science and Engineering, Shaanxi University of Technology, Hanzhong 723001, Shaanxi, China

[b]State Key Laboratory for Mechanical Behavior of Materials, Xi'an Jiaotong University, Xi'an 710049, Shaanxi, China

[c]Department of Physics, Department of Materials Science and Engineering, and Department of Biomedical Engineering, City University of Hong Kong, Tat Chee Avenue, Kowloon, Hong Kong, China

[d]Natural Active Industrialization Engineering Technology Research Centre of Shaanxi Province, Shaanxi University of Technology, Hanzhong 723001, Shaanxi, China

[e]College of Physics and Information Technology, Shaanxi Normal University, Xi'an 710062, Shaanxi, China

*Address correspondence to: zhanglizhai0512@snut.edu.cn (L. Z. Zhang); aitaotao0116@126.com (T. T. Ai); paul.chu@cityu.edu.hk (P. K. Chu)

The O 1s spectrum in Figure 6b shows peaks at about 528.76 eV, 530.96 eV, and 532.89 eV are assigned to Ce-O, O_v, and adsorbed oxygen (O_{ads}), respectively." In the analysis of O1s spectrum, authors have attributed peak at 530.96 eV to the oxygen vacancies. Core and valence level spectroscopy rely on the removal of an electron from an atom and measuring its kinetic energy by a spectrometer. In simple words, for O1s signal to be observed, one needs to have an oxygen atom in the lattice. When oxygen atom is absent (so called oxygen vacancy), then how come one can still obtain such signal? Therefore, XPS analysis require explanation from authors.

Answer: As the Ov is produced, the local electronic structure of surrounding oxygen atoms would be changed. Although the XPS couldn't directly detect missing oxygen atoms, it could indirectly reflect the existence of O_v through detecting the chemical state changes of surrounding oxygen atoms. Thereby, when splitting peaks of oxygen, the peaks at about 531.26 eV would be attributed to the O_v.

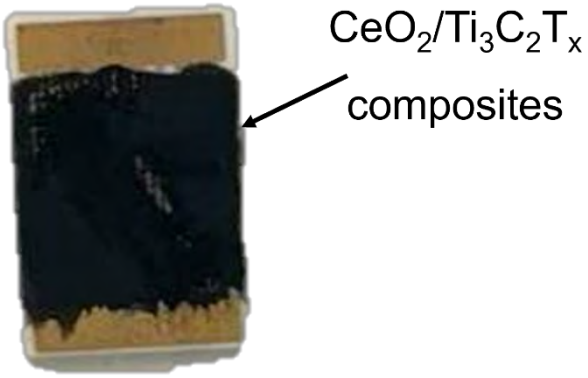

Figure S1 The photo of Au interdigital electrodes which is coated by $CeO_2/Ti_3C_2T_x$ composites.

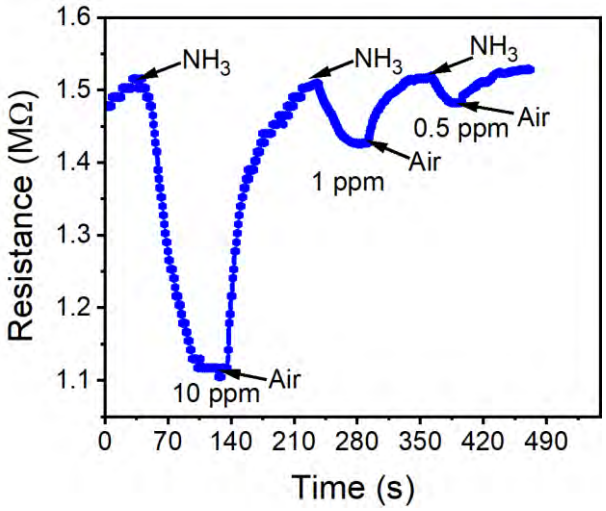

Figure S2. The response and recovery curve of Ce-Ti-b sensor toward 10 ppm, 1 ppm and 500 ppb NH_3 at RT.

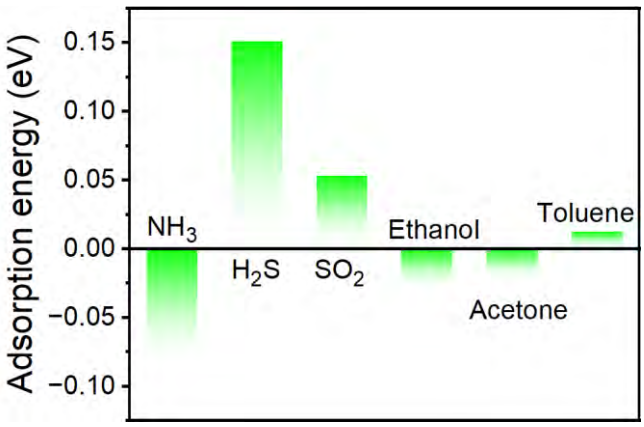

Figure S3. The adsorption energy of CeO_2 toward NH_3, H_2S, SO_2, ethanol, acetone and toluene.

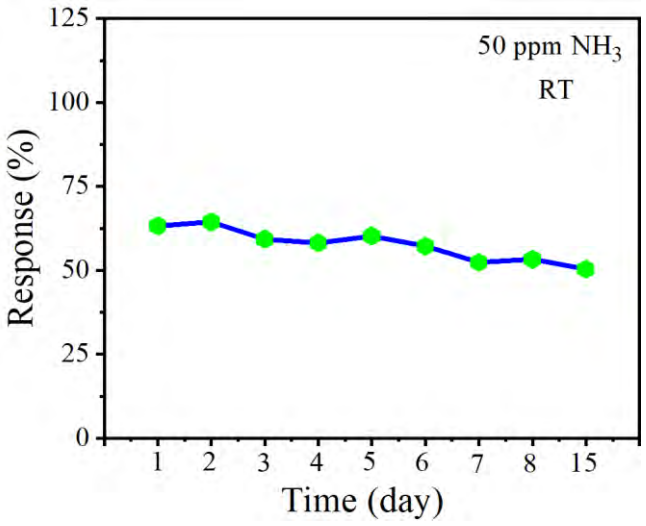

Figure S4. Response of Ce-Ti-b sensor to 50 ppm NH_3 after storage for two weeks

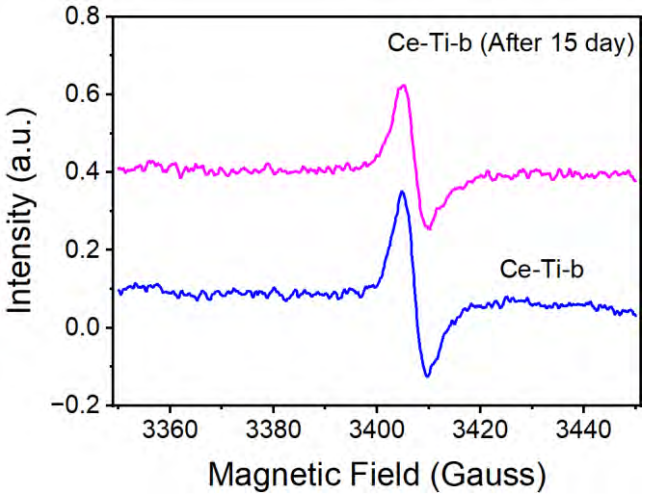

Figure S5. The EPR curves of CeO_2 and $Ti_3C_2T_x$ composites (Ce-Ti-b) before and after 15 days.

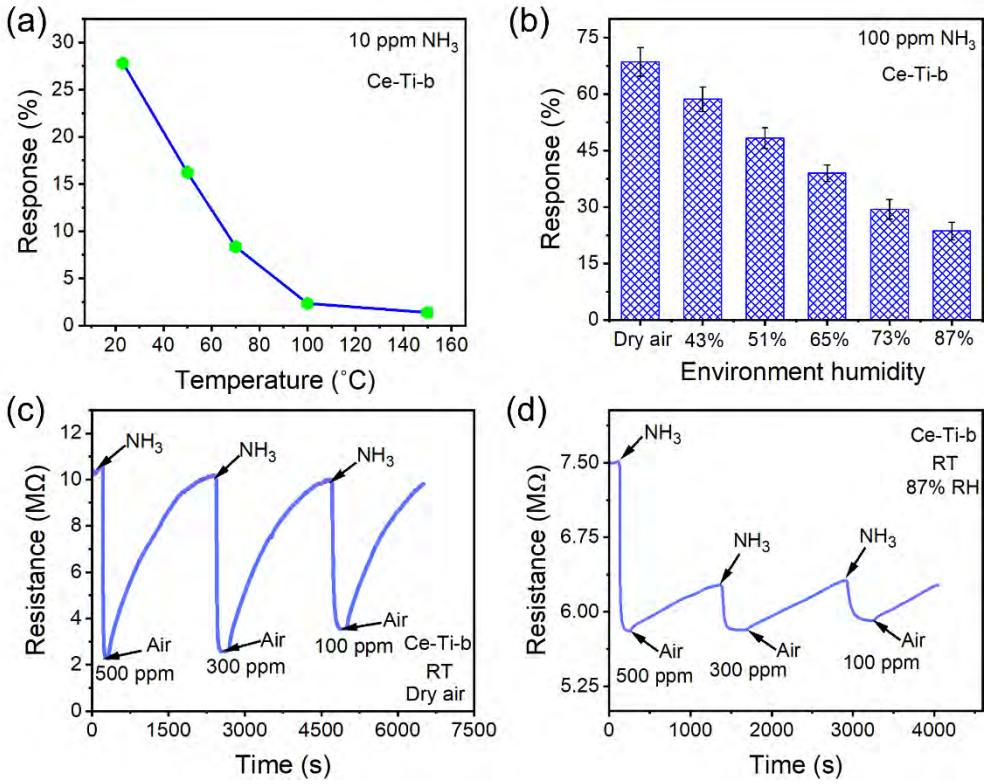

Figure S6. Response of the Ce-Ti-b sensor to 10 ppm NH_3 at different (a)Temperature and (b) Humidity; The resistance change curves of Ce-Ti-b sensor toward 500 ppm, 300 ppm and 100 ppm NH_3 in (c) dry air and (d) 87% RH humidity.

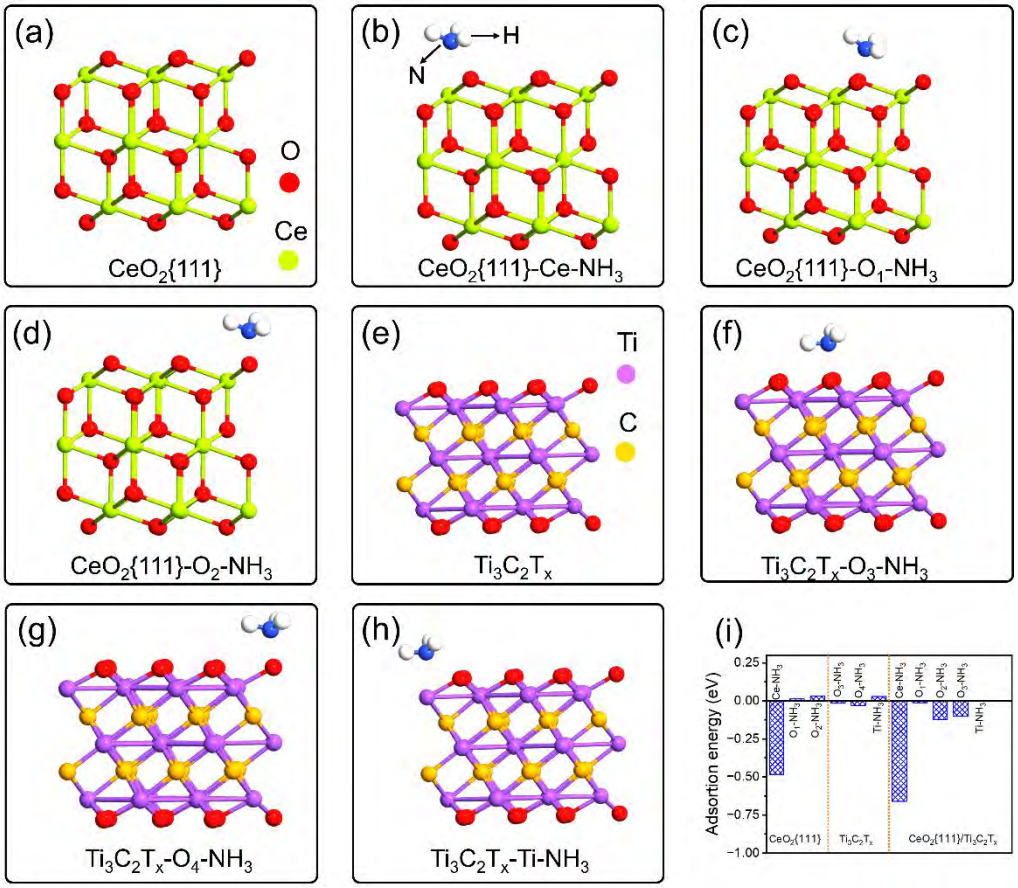

Figure S7 (a) The atom structure of CeO_2{111} facet; (b-d) the bonding configurations of NH_3 on Ce atom, O1 atom and O2 atom sites of CeO_2{111} facet, respectively. (e) the structure of $Ti_3C_2T_x$, (f-h) the bonding configurations of NH_3 on O1 atom, O2 atom and Ti atom of $Ti_3C_2T_x$; (i) The adsorption energy of NH_3 molecular on the surface of CeO_2, $Ti_3C_2T_x$ and CeO_2/ $Ti_3C_2T_x$ composites.

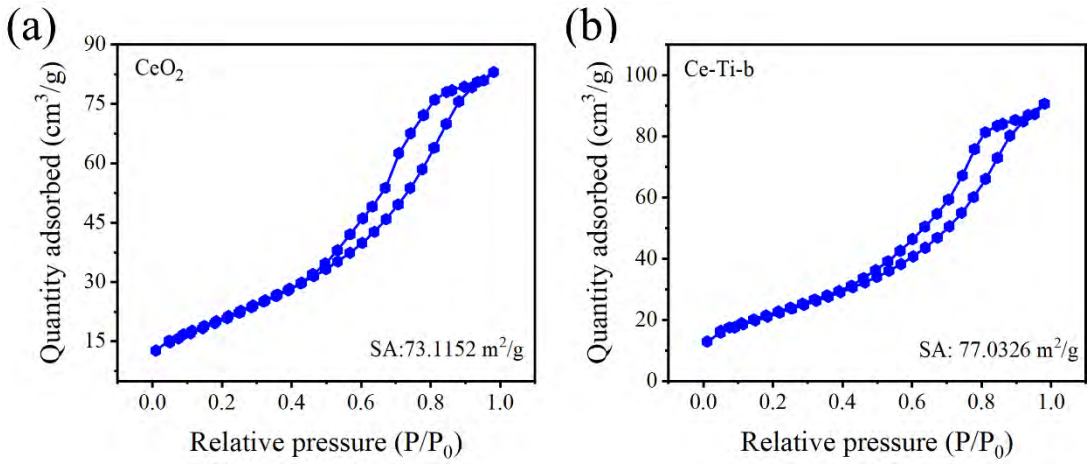

Figure S8 The BET surface area of (a) CeO_2 and (b) Ce-Ti-b.

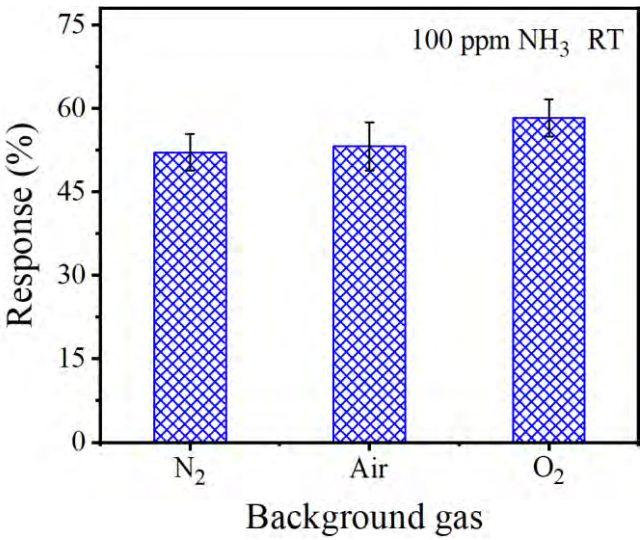

Figure S9. The response of Ce-Ti-b sensor toward 100 ppm NH_3 at RT in the different background gas.

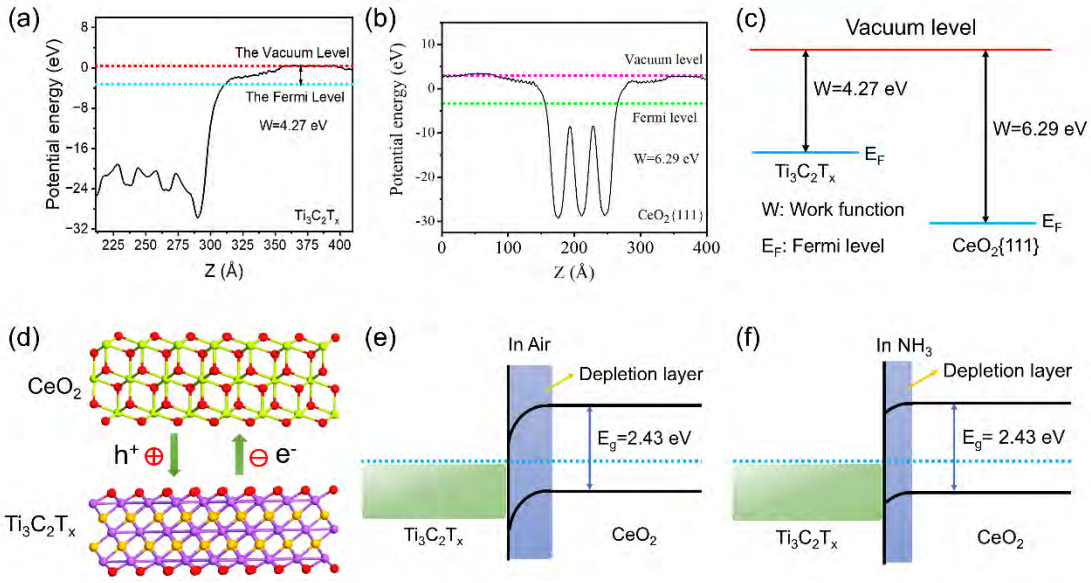

Figure S10. The work function of (a) $Ti_3C_2T_x$ and (b) CeO_2; (c) Schematic diagram of the work functions of CeO_2 and $Ti_3C_2T_x$; (d) Schematic diagram of charge carriers transfer; The variation in band structure of $Ti_3C_2T_x$ and CeO_2 heterojunction in (e) air and (f) NH_3.

Table S1. Comparison of NH_3-sensing performance of $CeO_2/Ti_3C_2T_x$ composites in this work with those in the previous work.

Sensing materials	concentration (ppm)	Response/recovery time (s)	Temperature (℃)	Response (%)	Ref.
$Ti_3C_2T_x$	500	120/230	RT	6.13	[14]
$Ti_3C_2T_x$	100	300/900	RT	0.8	[41]
$Ti_3C_2T_x$	100	240/360	RT	21%	[12]
3D-$Ti_3C_2T_x$	50	180/476	RT	0.8	[42]
Alkalized-Ti_3C_2	100	48/196	RT	28.87	[15]
$Ti_3C_2T_x$/ZnO	1000	34/103	RT	28.89	[43]
MXene/CuO	100	43/260	RT	24.8	[44]
$Ti_3C_2T_x/TiO_2$	10	33/277	RT	3.1	[45]
$Ti_3C_2T_x/TiO_2$	0.08	69/895	31	7.98	[46]
$CeO_2/Ti_3C_2T_x$ composites	10	147/875	RT	28.36	In this work

Response: $S_g = \frac{|R_g - R_a|}{R_a} \times 100$